Applied Physics A (2021) 127:704
https://doi.org/10.1007/s00339-021-04810-4

Applied Physics A
Materials Science & Processing

Micro-mechanical analysis of shape memory based engines

Yanlin Chen[1] · **Bernard Ricardo**[1]

Received: 1 June 2021 / Accepted: 28 July 2021 / Published online: 24 August 2021

Abstract
In this manuscript, we provide an analysis on the use of shape memory alloys (SMA), specifically NiTiNOL (Nickel–Titanium alloy, Naval Ordnance Laboratory), in a simple engine operating between two thermal reservoirs, constructed by looping a nitinol wire coil about two pulleys with their axes located at some distance from each other: when one end of a pulley is placed in hot water, the wire will tend to straighten, causing the pulleys to rotate. A qualitative explanation of the phenomenon (rotation of pulleys) with reference to the shape memory effect is given, and a quantitative model is constructed to predict the angular velocity of rotation. The accuracy of the model is then validated with experimental results. Beyond predicting behaviors of SMA-based engines, these results provide novel insight into the microscopic phase transformations occurring within a SMA, which is crucial in predicting the behavior of SMA subject to complex forms of thermomechanical stress, such as in temperature-sensitive actuators and catheter shafts.

Keywords Micro-mechanical · Shape memory · Engines · Thermodynamics

1 Introduction

In shape memory alloys (SMA), monoclinic multi-variant martensite (M) undergoes detwinning, instead of irreversible deformation, and transforms into single-variant martensite (S) with the application of an external stress. Transformations between the martensitic and austenitic phase are termed the "Shape Memory Effect", where both single and multi-variant martensitic fractions assume the interpenetrating simple cubic structure, austenite (A), as temperature is raised beyond the austenite start temperature, then reverts back to multi-variant martensite as temperature is lowered [1].

The significance of SMA lies in these reversible phase transformations, which allow low-grade thermal energy to be converted into mechanical work [2]. The molecular dynamics method was developed to investigate material properties and dynamic behavior on an atomistic scale, by numerically solving Newton's equation of motion for individual atoms [3]; using this method, martenistic transformations for nitinol were simulated by Sato et al. [4] in 2004 and Ackland et al. [5] in 2008. The ability of SMA to undergo phase transformation gives them a large recoverable strain and high capacity to dissipate energy, which makes them highly attractive for impact damping, seismic protection or health monitoring for impact damage detection [6]. Furthermore, SMAs also have applications in thermal engines, temperature-sensitive actuators, such as thermal valves for fluidics, catheter shafts for medical stents for its kink resistance, torquability, and biocompatibility, and in orthodontics for dental braces [7]. Consequently, in order to achieve precise control and predictive power over systems incorporating such materials, despite nonlinearities caused by the hysterisis associated with the shape memory effect, research has been conducted to understand and model these hystersis behavior [8].

The concept of constructing an engine using SMA was first introduced in the 1970s by Ridgway Banks at Lawrence Berkeley National Laboratory [9]. Since then, numerous works have been done to produce a constitutive model of SMA heat engines that employs various operation principles, namely offset crank engines, turbine engines, field engines, and miscellaneous [10]. However, existing works do not consider the phase transformations that lead to the macroscopic shape memory effect, instead focusing on the temperature and strain values along an engine cycle, to compute the work

✉ Yanlin Chen
h1710016@nushigh.edu.sg

[1] National University of Singapore High School of Mathematics and Science, 20 Clementi Avenue 1, Singapore 129957, Singapore

per unit mass [2, 11]. In addition, constitutive models focusing on the shape memory material itself, such as Chemisky et al. [12], aim to predict the macroscopic behaviour purely based on the thermodynamics of the process, while others, including Rizzoni et al. [13], consider the bending and recovery process of an isolated nitinol strip and hence does not consider the effects of mechanical coupling. Auricchio et al. consider the microscopic phase transformations that occur, which leads to macroscopic changes based on physical conditions; however, a complex return-map algorithm greatly increases the computational requirement, and the lack of an analytic model decreases the physical insight that could be obtained. Hence, this paper seeks to provide a constitutive model that predicts both the thermomechanical conditions, as well as the volume fraction distribution using a time-independent model.

The SMA-based engine investigated in this paper is constructed by looping a nitinol wire about two pulleys, one of which is immersed in hot water, as shown in Fig. 1. Here, nitinol is used as it is the most prevalent SMA [14].

2 Shape memory effect

We first elaborate on the microscopic changes that lead to the shape memory effect. The micromechanical changes during phase transformations are caused by external heat and stress. With the application of external stress via bending, an internal stress is induced, which produces a bending moment that acts in opposition to the deformation. Multi-variant martensite is detwinned into single-variant martensite to relieve the strain, causing the internal stress to decrease proportional to the fraction of single-variant martensite, limited by the maximum recoverable strain. Since stress is reduced, single-variant martensite does not revert back to multi-variant martensite even after the external force is removed. In heating, the increase in austenite reduces the volume fraction of both martensitic phases. This increases the internal stress and as a result bending moment, causing the wire to tend towards its trained shape. Upon cooling, austenite converts to multi-variant austenite.

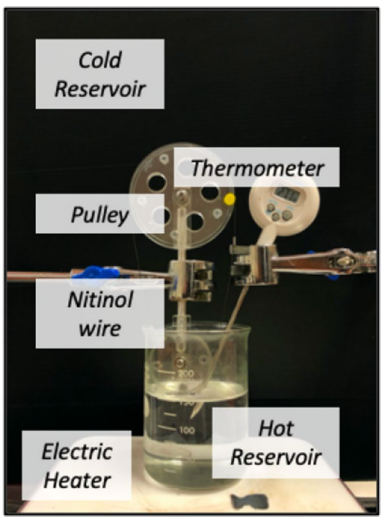

Fig. 1 Image of experimental setup

The ability of nitinol to undergo phase transformations provides a pathway for energy conversions. Under the assumption that the wire shape remains constant at steady state, the strain energy is hence constant. This is equal to the rotational kinetic energy of the wire and pulleys. However, we note the presence of air drag and frictional forces in the bearings of the pulley, and this work done by non-conservative forces is contributed by the heat energy from the water, via energy conversions to internal energy, from an increase in austenite phase. A no-slip condition is imposed between the wire and pulleys, resulting in a non-dissipative static friction.

3 Quantitative model

In the quantitative model, we first determine the strain profile along the wire. Batista [15] considered the use of elliptic functions the wire shape from two equal pulleys, where the system is symmetrical about both the x and y axis. From the case where the rod is subjected to a terminal conservative force, we develop on this to solve for the wire shape around two unequal pulleys. This is validated with experimental footage. The temperature profile is then determined from Newton's Law of Cooling. The volume fraction is the key to finding the angular velocity, yet it is itself dependent on the velocity, which affects the temperature profile. Thus, given the recursive dependence on velocity, we use conservation of energy as a constraint, to solve for the equilibrium velocity, choosing the equality between the increase in internal energy (through the addition of latent energy for phase transformation; increase in A phase) and decrease in strain energy (reduction in S phase).

3.1 Wire shape

Referring to Fig. 2, let $s = 0$ be the point where the wire first comes into contact with the water, where s is the arc-length coordinate. Here, the critical points s_1, s_2, s_3, and s_4 are where the wire comes into or loses contact with the respective pulley, and ℓ is the length of wire. θ_1^* and θ_2^* are the critical angles from the y-axis to points s_2 and s_1, respectively. (Note that the engine is symmetrical about the y-axis.) d is the distance between the centres of pulleys, and R_1 and R_2 are the radii of the top and bottom pulley, respectively.

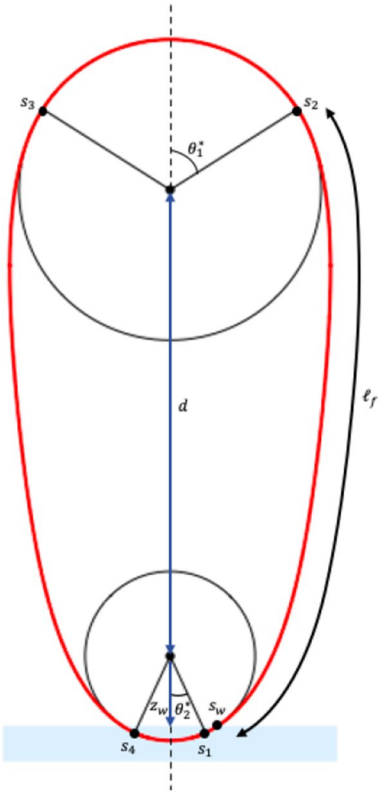

Fig. 2 Labelled engine diagram with theoretically computed wire shape

The wire shape is modelled by considering half of the engine (right side), as a beam of length ℓ_f (length of free segment) with a single point of contact at s_1, which experiences a terminal conservative force directed at an angle α, such that it comes into contact with the top pulley at s_2. The elliptic modulus (eccentricity) will be k. Since the wire is continuous, the x, y coordinates of end of free segment need to match with coordinates of critical points; additionally, angle and curvature χ need also be conserved. The boundary condition can now be written as:

$$\begin{aligned} \theta[0] &= \theta_2^* & \theta[1] &= \pi - \theta_1^* \\ \chi[0] &= 1/R_2 & \chi[1] &= 1/R_1 \\ x[0] &= R_2 \sin[\theta_2^*] & x[1] &= R_1 \sin[\theta_1^*] \\ y[0] &= -R_2 \cos[\theta_2^*] & y[1] &= d + R_1 \cos[\theta_2^*] \end{aligned}$$

From Batista [15], the equations based on $\sigma = s/\ell_f$, the normalised arc length parameter, are

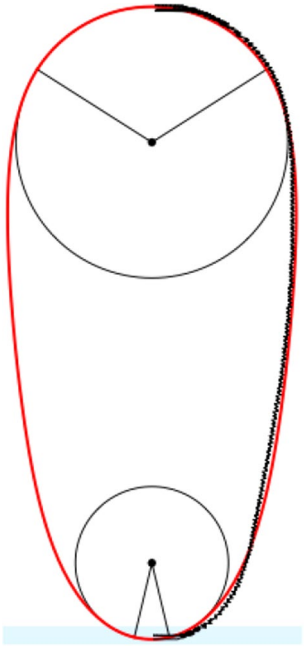

Fig. 3 Theoretically predicted wire shape from solving solving Eq. (3.1) with boundary conditions (red line) versus experimental wire shape (black)

$$\begin{aligned} \theta &= -\alpha + \mathrm{am}[c + k\omega\sigma, k^{-1}] \\ \chi &= 2\ell_f^{-1}\omega k \mathrm{dn}[c + k\omega\sigma, k^{-1}] \\ x &= x_o + \ell_f(\boldsymbol{a}\ \cos\ \alpha + \boldsymbol{b}\ \sin\ \alpha) \\ y &= y_o + \ell_f(-\boldsymbol{a}\ \sin\ \alpha + \boldsymbol{b}\ \cos\ \alpha) \end{aligned} \tag{3.1}$$

where am is the Jacobi amplitude function, and

$$\begin{aligned} \boldsymbol{a} &= \frac{2k}{\omega}\left(\epsilon[c + k\omega\sigma, k^{-1}] - \epsilon[c, k^{-1}]\right) - (2k^2 - 1)\sigma \\ \boldsymbol{b} &= \frac{2k}{\omega}(\epsilon[c, k^{-1}] - \epsilon[c + k\omega\sigma, k^{-1}]) \end{aligned}$$

and χ is the curvature defined on the normalised arc length parameter. Then, we use the boundary conditions to solve for the 4 unknown parameters $(\alpha, \theta_1^*, \theta_2^*, k)$ and 2 unknown functions (ω, c). To verify the accuracy of the theoretical prediction (red), the plotted parametric equations are overlayed with the experimental wire shape (black) that is extracted from experimental footage, using image binarisation and edge-detection mechanisms, as shown in Fig. 3.

We note that near the bottom pulley, where the radius of curvature is larger, the actual flexural rigidity YI of the wire (from experimental footage: black) is greater than the predicted value (from predicted shape: red). This is due to the assumption of a linear relationship between the bending moment M and curvature in Batista's model, that is given by,

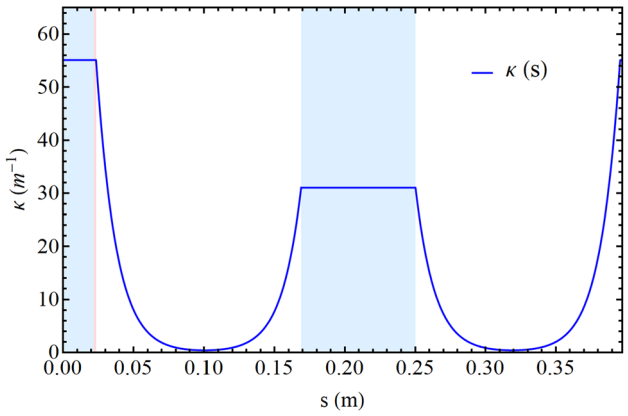

Fig. 4 Plot of curvature against arc-length coordinate s

$$M = YI\left(\kappa - \frac{1}{R_o}\right)$$

however, this assumption is not valid in the case of SMAs [16], where the flexural rigidity is greater than the linear approximation at low and high values of strain, which agrees with the deviation that we have noted. Despite this, we see a reasonably good fit between theory and experiment (Fig. 3), and hence, the approximation is valid in this case. Here, the experimental wire shape is obtained from the binarisation and processing of an image of the engine, with the wire looped about the pulleys. Knowing the curvature along the free segment, we can write the piecewise equation for curvature along the wire. The graph of curvature against the arc-length coordinate is shown in Fig. 4.

$$\kappa[s] = \begin{cases} 1/R_2 & \text{if } s \le s_1 || s \ge s_4 \\ \chi\left[\frac{(s-s_1)}{\ell_f}\right] & \text{if } s < s_2 \\ 1/R_1 & \text{if } s_2 \le s \le s_3 \\ \chi\left[\frac{(s_4-s)}{\ell_f}\right] & \text{if } s < s_4 \end{cases} \tag{3.2}$$

The strain $\epsilon = z/R$ can thus be expressed as

$$\epsilon[s] = z\left(\frac{1}{R_o} - \kappa[s]\right) \tag{3.3}$$

where z is the thickness coordinate across the cross section of the wire measured from the centreline, and R_o is the radius of curvature of the trained wire shape. We note the plot of $\kappa[s]$ (Fig. 4), where the shaded regions denotes the segments of wire in contact with the pulley.

3.2 Temperature profile

Next, we consider the temperature distribution along the wire. From Fourier's Law,

$$\frac{DQ}{Dt} = -k\vec{\nabla}T = -kA\frac{\mathrm{d}T}{\mathrm{d}x}$$

where D/Dt is the material derivative, and k is the conductive heat transfer coefficient of martensite (k_M) or austenite (k_A). Considering Newton's Law of Cooling,

$$\rho c\dot{x}\frac{\partial T}{\partial s} - k\frac{\partial^2 T}{\partial s^2} + \frac{h(T_o - T)}{\tau} = 0 \tag{3.4}$$

where h is the convective heat transfer coefficient in air (h_a) or water (h_w), and T_o is the temperature of the hot (T_w) or cold (T_a) reservoir.

$$h = \begin{cases} h_w & \text{if } s < s_w || s = \ell \\ h_a & \text{if } s \ge s_w \end{cases}$$

$$k = \begin{cases} k_A & \text{if } s < s_w || s = \ell \\ k_M & \text{if } s \ge s_w \end{cases}$$

$$T_o = \begin{cases} T_w & \text{if } s < s_w || s = \ell \\ T_a & \text{if } s \ge s_w \end{cases}$$

Numerical finite-difference method is used to solve for the temperature profile, which is shown in Fig. 5. Heating occurs in the red region, when the wire is in contact with the hot reservoir, while cooling occurs in the grey area, where the wire is in the cold reservoir (air).

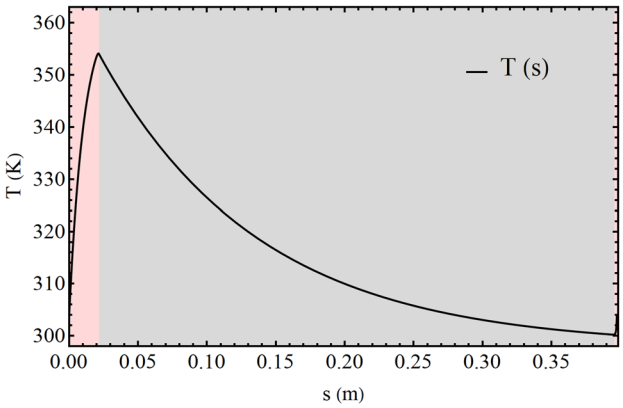

Fig. 5 Plot of temperature against arc-length coordinate s for $v = 0.38$ m/s ($\omega = 11.8$ rad/s)

3.3 Volume fraction distribution

The strain and temperature profile are used to determine the volume fraction. Auricchio et al. [17] introduced a complex return-map algorithm to solve the time-discrete rate evolution equations. Here, we integrate their time-dependent equations to produce time-stationary equations describing the volume fraction evolution in a wire loop subject to first bending, and subsequently free recovery from heating.

$$\text{In bending, if } \left(\frac{\sigma_s^{AS}}{Y_S}+\epsilon_L\xi_S\right) \le |\epsilon| \le \left(\frac{\sigma_f^{AS}}{Y_S}+\epsilon_L\right)$$

$$\xi_S^{B1} = 1 - \left(\frac{|\epsilon| - \left(\frac{\sigma_f^{AS}}{Y_S}+\epsilon_L\right)}{|\epsilon_i| - \left(\frac{\sigma_f^{AS}}{Y_S}+\epsilon_L\right)}\right) \tag{3.5}$$

$$\xi_M^{B1} = \left(\frac{|\epsilon| - \left(\frac{\sigma_f^{AS}}{Y_S}+\epsilon_L\right)}{|\epsilon_i| - \left(\frac{\sigma_f^{AS}}{Y_S}+\epsilon_L\right)}\right) \tag{3.6}$$

In heating, if $T \ge T_s^{SA}$,

$$\xi_S^{H2} = \left(\frac{|\epsilon| - \frac{C^{SA}\left(T-T_f^{SA}\right)}{Y_A}}{|\epsilon_i| - \frac{C^{SA}\left(T_a-T_f^{SA}\right)}{Y_A}}\right)\xi_S^{B1} \tag{3.7}$$

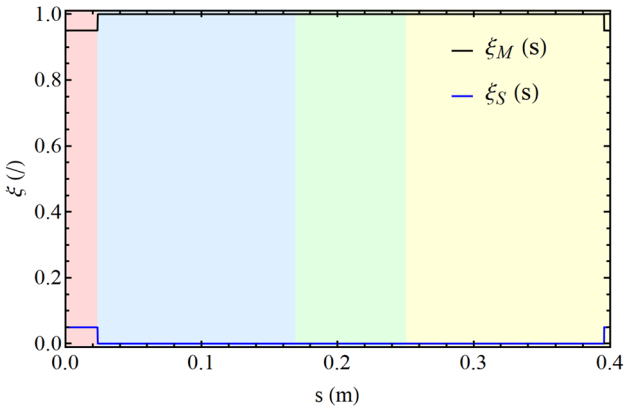

Fig. 6 Volume fraction of S, M phase following bending

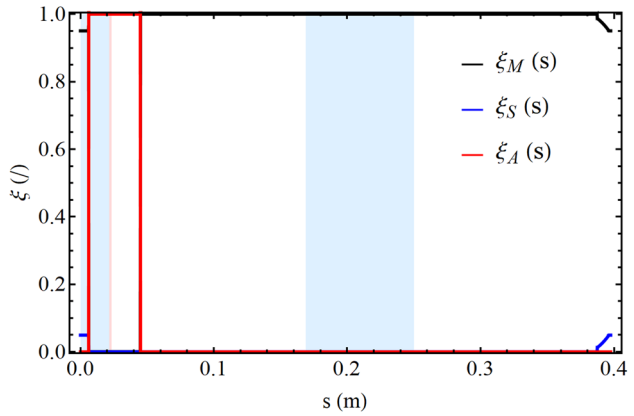

Fig. 7 Volume fraction of S, M, A phase following heating

$$\xi_M^{H2} = \left(\frac{|\epsilon| - \frac{C^{SA}\left(T-T_f^{SA}\right)}{Y_A}}{|\epsilon_i| - \frac{C^{SA}\left(T_a-T_f^{SA}\right)}{Y_A}}\right)\xi_M^{B1} \tag{3.8}$$

Here, ξ is the volume fraction, σ is the transformation stress, Y the Young's modulus, ϵ_L the maximum recoverable strain, ϵ_i the initial strain present in the wire loop, and C the Clausius–Clapeyron constant. The superscript refers to the process: AS represents transformation from austenite to single-variant martensite, $B1$ and $H2$ the bending and heating process. The subscript S, M and A represent the three phases, while s and f refer to the start or final values of the process. For instance, σ_s^{AS} is the start stress for transformation from austenite to single-variant martensite.

From this, we obtain the plot of the volume fraction following bending (Fig. 6) and heating (Fig. 7), across the arc-length coordinate s, integrated across the thickness coordinate z, where multi-variant martensite is represented by the black line, single-variant martensite blue, and austenite red. In this calculation, strain is used in the place of stress; as a result, the nonlinearity of the flexural rigidity only impacts the volume fraction distribution via the prediction of the wire shape.

3.4 Equilibrium velocity

Knowing the specific latent heat, the change in volume fraction can give the energy required for phase transformation, in addition to change in strain energy. Note that $\xi[s,z]$, $\epsilon[s,z]$, and $T[s,z]$ are dependent on the velocity of the wire (the

dependency has been eliminated for clarity); hence, to find the equilibrium (actual) $\dot{x}$, we use conservation of energy as the constraint, where increase in internal energy due to phase transformation E_{PT} equals the decrease in strain energy ΔU.

$$\int_0^{\ell} \rho\left(\pi\tau^2\ell\right) L_t\left(\xi_S^{H2} + \xi_M^{H2} - \xi_S^{B1} - \xi_M^{B1}\right) ds = \int_0^{\tau}\int_0^{\ell}\int_0^{\epsilon_L} \sigma \, d\epsilon \, \mathrm{d}s \, \mathrm{d}z - U_i \tag{3.9}$$

where from Rizzoni et al. [13],

$$\sigma = \begin{cases} Y\left(\epsilon - \epsilon_L \xi_s\right) \text{ if } \epsilon \geq 0 \\ Y\left(\epsilon + \epsilon_L \xi_s\right) \text{ otherwise} \end{cases}$$

and U_i is the initial strain energy when the volume fraction of single-variant martensite is zero.

3.5 Methods

The computational procedure to obtain the angular velocity is as follows: where v is the equilibrium velocity, and the degree of precision is controlled by ϵ_r [18]. Mathematica `findRoot` is used to find the solution.

Algorithm 1: Root-finding Procedure

```
initialization;
f(v) = E_PT − ΔU = 0;
compute strain profile ϵ;
while abs(h) ≥ ϵ_r do
    for elements on arc-length s do
        compute temperature profile T;
        if bending condition fulfilled then
            compute ξ_s^B1 and ξ_M^B1;
        else
            ξ_s^B1 = ξ_{s,o};
            ξ_M^B1 = ξ_{M,o};
        end
        if heating condition fulfilled then
            compute ξ_s^H2 and ξ_M^H2;
        else
            ξ_s^H2 = ξ_s^B1;
            ξ_M^H2 = ξ_M^B1;
        end
        compute E_PT and ΔU;
    end
    h = f(v) / f'(v);
    v = v − h;
end
```

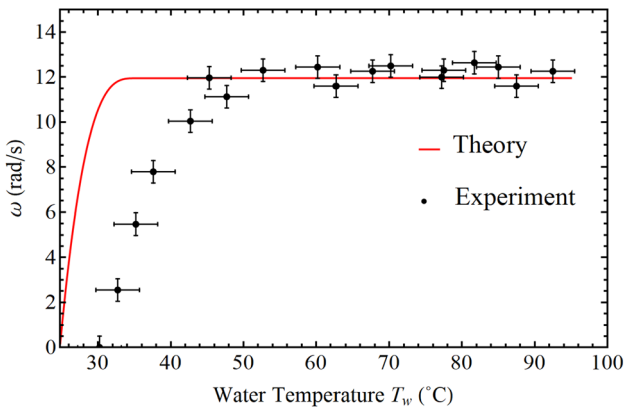

Fig. 8 Graph of angular velocity against temperature of hot reservoir: black experimental points, red theoretical prediction

4 Results and discussion

4.1 Experimental validation

The experimental results achieved are shown for angular velocity against temperature of the hot reservoir in Fig. 8. Tracker is used to give the displacement-time data from the 120 frames-per-second footage, and a fast-fourier transformation is used to give the frequency in Hertz. For certain experimental points, the angular velocity is determined from the period. The uncertainty associated with the temperature is a result of fluctuations due to convection, and errors in angular velocity are based on the median frequency resolution. There exists a 5° C deviation in temperature between experimental and theoretical values, before the maximum angular velocity is reached. This is attributed to the difference in phase transformation temperatures for S and M phase, as shown by the phase plot (Fig. 10). Since a small percentage (Fig. 6) of volume fraction in contact with the hot reservoir initially existed as S phase, this results in a lower predicted value of austenite-start and final temperature than the actual value.

For the graph of angular velocity against distance beneath water surface (Fig. 9), we note an increase in ω

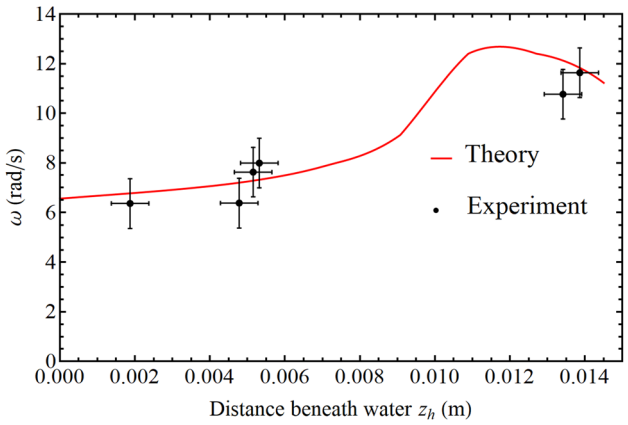

Fig. 9 Graph of angular velocity against distance beneath water surface: black experimental points, red theoretical prediction

as z_h increases, due to a greater heat transfer that allows for a greater fraction of conversion to austenite phase, till a threshold at $z_h \approx 0.011$ m where the angular velocity decreases, when fraction of conversion decreases from an increase in S phase (which requires a high temperature for phase transformation) and decrease in M phase. Horizontal error bars arise from possible parallex error in determining distance using Tracker.

4.2 Further insights: efficiency

We consider the thermal efficiency of the engine, which is given by

$$\eta = \frac{\text{power dissipated } (R)}{\text{net heat input } (\int \dot{q}\, \mathrm{d}s)}, \text{ where}$$

$$\int \dot{q}\, \mathrm{d}s = \int_0^{\ell} 2\pi\, h[s]\, (T_o[s] - T[s])\, \mathrm{d}s$$

and based on the Rayleigh dissipation function,

$$R = \dot{x}\left(\frac{k_{f1}}{R_1} + \frac{k_{f2}}{R_2}\right) + \frac{\dot{x}^2}{2}\left(\frac{k_{s1}}{R_1^2} + \frac{k_{s2}}{R_2^2}\right)$$

Hence, we are able to obtain the graph of efficiency against temperature of the hot reservoir (Fig. 11). We note the the maximum efficiency of 8%; in comparison, conventional 2-stroke gasoline engines have a typical thermal efficiency of 22% [19]. To understand the differences in efficiency, we realise that unlike in a conventional engine, the driving mechanism of the nitinol engine is derived from the continuous heat gain from the water and heat loss to the air. As such, the main source of energy (or power) loss is the significant loss of heat, which is not converted to energy used to overcome non-conservative force, from the wire to the cold reservoir.

4.3 Further insights: energy curves

Next, an engine should be able to carry a load. We investigated the effect of varying distance beneath water surface on the rotational kinetic energy at steady state, for varying mass of the loads (Fig. 12). The setup image is shown in Fig. 13. In this nitinol engine, the angular velocity is found by equating the increase in internal energy with the decrease in strain energy, both of which depends only on the temperature and strain profile. Similarly, in this

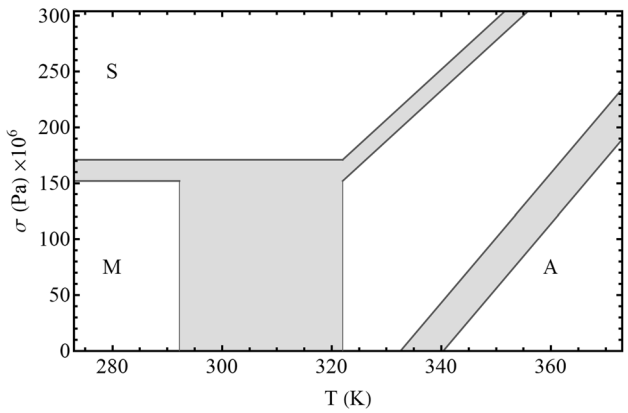

Fig. 10 Characterised stress-temperature phase plot

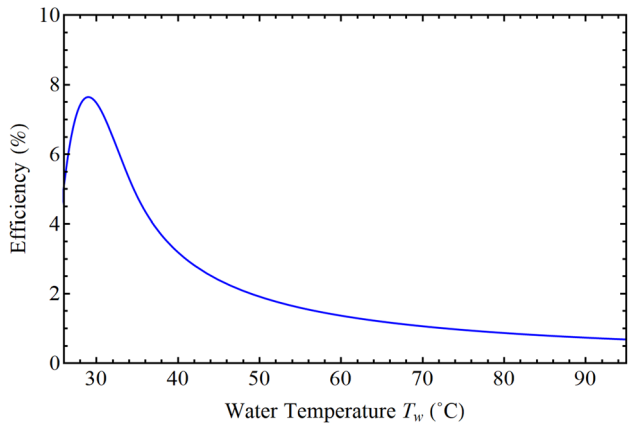

Fig. 11 Theoretical graph of efficiency against temperature of hot reservoir

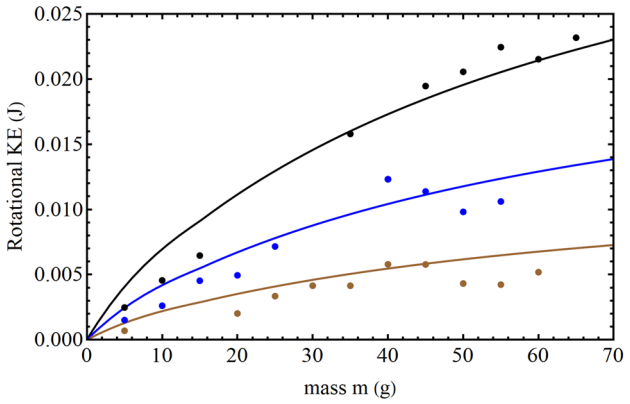

Fig. 12 Graph of rotational kinetic energy against distance beneath water surface (experimental points, theoretical lines): $z_h = -0.0117$m, black, $z_h = -0.0152$m, blue, $z_h = -0.0044$m, brown

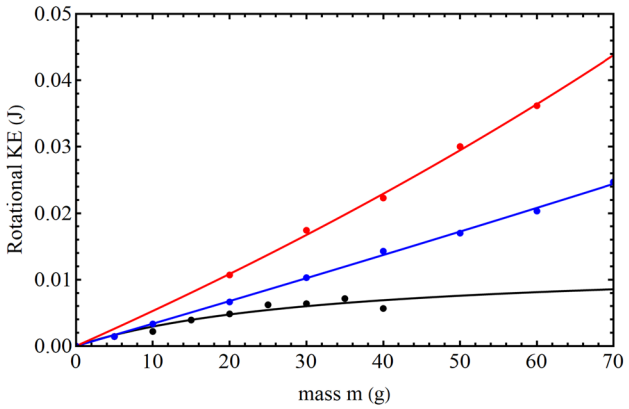

Fig. 14 Graph of rotational kinetic energy against distance between pulleys (experimental points, best fit line): $d = 0.11$m, red. $d = 0.102$m, blue. $d = 0.12$m, black

system, kinetic energy equals the strain energy, which is independent of mass. Hence, as mass increases, the angular velocity has to decrease for kinetic energy to remain constant. Thus, the rotational kinetic energy of the mass can be expressed as:

$$KE = \frac{1}{2} I_{\text{mass}} \frac{I_{\text{pulley}}}{I_{\text{pulley}} + I_{\text{mass}}} \omega^2$$

where I_{pulley} is the moment of inertia of the pulley only.

Considering the data for varying distance between pulleys (Fig. 14), we realise that there exists an optiminal distance between pulleys for maximum rotational kinetic energy. As the distance increases beyond this optiminal point (black), the engine is unable to turn due to the strong normal and tension forces exerted by the wires, leading to a low value of rotational kinetic energy. However, when the distance between pulleys is small such that the wire becomes slacker (red), the change in strain is less, which also leads to a drop in kinetic energy.

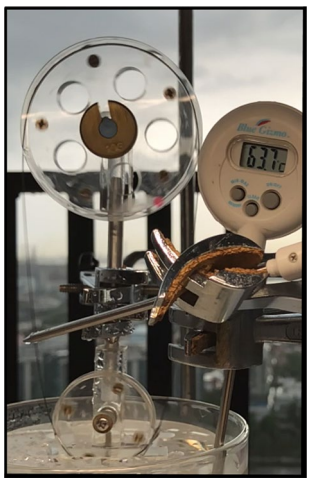

Fig. 13 Image of setup used to obtain energy curves: circular weights are attached to the centre of the top pulley

5 Conclusion

In this manuscript, we analysed a simple nitinol engine that rotates when placed between two thermal reservoirs (water and air) and introduced a novel qualitative mechanism of the shape memory effect, as well as how the engine operates. Next, we proposed a micromechanical model considering the strain and temperature profile to predict the volume fraction distribution, in order to find the angular velocity of the rotation using energy conservation. Finally, we validated our theoretical predictions with experimental data and empirically investigated the effects of adding a load onto the engine. These results lead to an insightful understanding of how the engine (and shape memory materials) functions and provides a computationally non-intensive method of predicting behaviors of SMA under thermomechanical stress, thus increasing the scope of application of nitinol.

6 Future work

Further work can be done by considering a transformation temperature as a function of multi- and single-variant volume fractions, to achieve a more accurate prediction at temperatures close to the austenite start temperature. Furthermore, an investigation can be conducted on the effect of varying the distance between pulleys, which will likely demonstrate the presence of an optimum value of distance between pulleys for maximum rotational kinetic energy (as

elaborated in Further Insights: Energy Curves) that will lead to greater insight on the nitinol engine.

Appendix

Wire shape derivation

Consider Fig. 15. Let $\alpha_1 = \cos^{-1}\left(\frac{|z_w|}{R_2}\right)$, z_w is the distance to water surface.

$s_w = 2R_2(\alpha)$ and $s_1 = R_2(\alpha + \theta_2^*)$

Similarly,

$s_2 = s_1 + \ell_f\ ,\ s_3 = s_2 + 2R_1(\theta_1^*)\ ,\ s_4 = s_3 + \ell_f$

From the equations for θ satisfying the boundary conditions, we determine the functions c and ω. When $\sigma = 0$, the wire just lost contact with the bottom pulley.

$\theta_2^* = -\alpha + 2\text{am}[c, k^{-1}]$

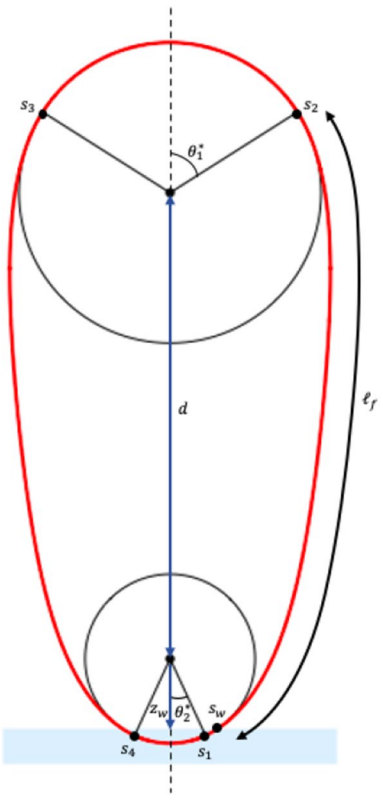

Fig. 15 Labelled engine diagram with theoretically computed wire shape

Hence,

$$c = F\left[\frac{\alpha + \theta_2^*}{2}, k^{-1}\right] \tag{7.1}$$

where the incomplete elliptic integral of the first kind F is the inverse of the Jacobi amplitude function am. Similarly

$\pi - \theta_1^* = -\alpha + 2\text{am}[c + k\omega, k^{-1}]$

Hence,

$$\omega = \frac{F\left[\frac{\alpha+\pi-\theta_2^*}{2}, k^{-1}\right] - c}{k} \tag{7.2}$$

Note that c and ω are functions of $\alpha, \theta_1^*, \theta_2^*, k$. Next, we consider the boundary conditions for χ. Based on

$$\frac{1}{R_2} = 2\left(\frac{2\pi R_w}{2} - R_1\theta_1^* - R_2\theta_2^*\right)^{-1} \omega k \text{dn}[c, k^{-1}]$$
$$\frac{1}{R_1} = 2\left(\frac{2\pi R_w}{2} - R_1\theta_1^* - R_2\theta_2^*\right) \omega k \text{dn}[c + k\omega, k^{-1}]$$

where $\ell = 2\pi R_w$ is the length of wire, we obtain

$$R_1 = \frac{\pi R_w \mathbf{dn}_1}{\theta_1^*\mathbf{dn}_1 + \theta_2^*\mathbf{dn}_2 + 2k\omega\ \mathbf{dn}_1 \cdot \mathbf{dn}_2} \tag{7.3}$$

$$R_2 = \frac{\pi R_w \mathbf{dn}_2}{\theta_1^*\mathbf{dn}_1 + \theta_2^*\mathbf{dn}_2 + 2k\omega\ \mathbf{dn}_1 \cdot \mathbf{dn}_2} \tag{7.4}$$

where

$\mathbf{dn}_1 = \text{dn}[c, k^{-1}],\ \mathbf{dn}_2 = \text{dn}[c + k\omega, k^{-1}]$

Finally, we see that

$$d + R_1\cos[\theta_2^*] = -R_2\cos[\theta_2^*] + \ell_f(-\boldsymbol{a}\ \sin[\alpha] + \boldsymbol{b}\ \cos[\alpha])$$
$$R_1\sin[\theta_1^*] = R_2\sin[\theta_2^*] + \ell_f(\boldsymbol{a}\ \cos[\alpha] + \boldsymbol{b}\ \sin[\alpha])$$

Simplifying,

$$x[1] = x[0] + \ell_f\left(\boldsymbol{a'}\cos[\alpha] + \boldsymbol{b'}\sin[\alpha]\right) \tag{7.5}$$

$$\delta = y[0] + \ell_f\left(-\boldsymbol{a'}\sin[\alpha] + \boldsymbol{b'}\cos[\alpha]\right) - R_1\cos[\theta_1^*] \tag{7.6}$$

where

$$\boldsymbol{a'} = \frac{2k}{\omega}\left(\epsilon[c + k\omega, k^{-1}] - \epsilon[c, k^{-1}]\right) - (2k^2 - 1)$$
$$\boldsymbol{b'} = \frac{2k}{\omega}(\text{dn}[c, k^{-1}] - \text{dn}[c + k\omega, k^{-1}])$$

We now have 4 equations (7.3, 7.4, 7.5, 7.6) that can be solved using Mathematica `findRoot` to find the 4 unknowns $k, \theta_1^*, \theta_2^*, \alpha$.

Temperature profile

Next, we consider the temperature distribution along the wire. From Fourier's Law,

$$\frac{DQ}{Dt} = -k\vec{\nabla}T = -kA\frac{\mathrm{d}T}{\mathrm{d}x}$$

Considering an infinitesimal segment of wire dx,

$$\begin{aligned}\frac{DQ}{Dt} &= (\rho A\mathrm{d}x)c\frac{DT}{Dt}\\ &= -kA\left.\frac{\mathrm{d}T}{\mathrm{d}x}\right|_x + kA\left.\frac{\mathrm{d}T}{\mathrm{d}x}\right|_{x+\mathrm{d}x} + \dot{q}\ \mathrm{d}x\\ \rho c\frac{DT}{Dt} &= \frac{kA\left.\frac{\mathrm{d}T}{\mathrm{d}x}\right|_{x+\mathrm{d}x} - kA\left.\frac{\mathrm{d}T}{\mathrm{d}x}\right|_x}{\mathrm{d}x} = k\frac{d^2T}{\mathrm{d}x^2} + \dot{q}(x)\end{aligned}$$

Given that $\frac{Dy}{Dt} = \frac{\partial y}{\partial t} + \vec{u}\cdot\vec{\nabla}y = \frac{\partial y}{\partial t} + \dot{x}\frac{\partial y}{\partial s}$,

$$\rho c\frac{DT}{Dt} = \rho c\Big(\frac{\partial T}{\partial t} + \dot{x}\frac{\partial T}{\partial s}\Big) = k\frac{d^2T}{\mathrm{d}x^2} + \dot{q}(x)$$

where $\dot{q} = h(T_o - T)$.

Volume fraction distribution

Knowing the strain and temperature profile, we use these information to determine the volume fraction at each point. From Auricchio et al., the rate evolution equations are given by

$$\begin{aligned}\dot{\xi}_S &= \dot{\xi}^{AS}_{S,1} + \dot{\xi}^{AS}_{S,2} + \dot{\xi}^{MS}_{S,1} + \dot{\xi}^{MS}_{S,2} + \dot{\xi}^{SA}_{S}\\ \dot{\xi}_M &= \dot{\xi}^{AM}_{M} + \dot{\xi}^{MS}_{M,1} + \dot{\xi}^{MS}_{M,2} + \dot{\xi}^{MA}_{M}\end{aligned}$$

where production of multi-variant martensite

$$\dot{\xi}^{AM}_M = \big(\xi_S + \xi_M - 1\big)\mathcal{H}^{AM}\frac{\dot{T}}{T - T^{AM}_f}$$

production of single-variant martensite

$$\begin{aligned}\dot{\xi}^{AS}_{S,1} &= \big(\xi_S + \xi_M - 1\big)\mathcal{H}^{AS}_1\frac{\dot{G}^{AS}_1}{G^{AS}_1 - S^{AS}_{f,1}}\\ \dot{\xi}^{AS}_{S,2} &= \big(\xi_S + \xi_M - 1\big)\mathcal{H}^{AS}_2\frac{\dot{G}^{AS}_2}{G^{AS}_2 - S^{AS}_{f,2}}\\ \dot{\xi}^{MS}_{M,1} &= \xi_M\mathcal{H}^{AS}_1\frac{\dot{G}^{AS}_1}{G^{AS}_1 - S^{AS}_{f,1}}\\ \dot{\xi}^{MS}_{M,2} &= \xi_M\mathcal{H}^{AS}_2\frac{\dot{G}^{AS}_2}{G^{AS}_2 - S^{AS}_{f,2}}\\ \dot{\xi}^{MS}_{S,1} &= -\xi_M\mathcal{H}^{AS}_1\frac{\dot{G}^{AS}_1}{G^{AS}_1 - S^{AS}_{f,1}}\\ \dot{\xi}^{MS}_{S,2} &= -\xi_M\mathcal{H}^{AS}_2\frac{\dot{G}^{AS}_2}{G^{AS}_2 - S^{AS}_{f,2}}\end{aligned}$$

production of austenite

$$\begin{aligned}\dot{\xi}^{SA}_S &= \xi_S\mathcal{H}^{SA}\frac{\dot{G}^{SA}}{G^{SA} - S^{AS}_{f,1}}\\ \dot{\xi}^{MA}_M &= \xi_M\mathcal{H}^{SA}\frac{\dot{G}^{SA}}{G^{SA} - S^{AS}_{f,1}}\end{aligned}$$

here, we define

$$\begin{aligned}S^{AS}_{s,1} &= \tfrac{R^{AS}_{s,1}}{Y} + \varepsilon_L\xi_s \quad S^{AS}_{f,1} = \tfrac{R^{AS}_{f,1}}{Y_S} + \varepsilon_L\\ S^{SA}_{s} &= \tfrac{R^{SA}_{s}}{Y} + \varepsilon_L\xi_s \quad S^{AS}_{s,2} = \tfrac{R^{AS}_{s,2}}{Y_S} + \varepsilon_L\xi_s\\ S^{AS}_{f,2} &= \tfrac{R^{AS}_{f,2}}{Y_S} + \varepsilon_L \quad S^{SA}_{f} = \tfrac{R^{SA}_{f}}{Y} + \varepsilon_L\end{aligned}$$

where

$$\begin{aligned}R^{AS}_{s,1} &= \sigma^{AS}_s \qquad R^{AS}_{f,1} = \sigma^{AS}_f\\ R^{SA}_{s} &= -C^{SA}T^{SA}_s \quad R^{AS}_{s,2} = \sigma^{AS}_s - C^{AS}T^{AS}_s\\ R^{AS}_{f,2} &= \sigma^{AS}_f - C^{AS}T^{AS}_s \quad R^{SA}_{f} = -C^{SA}T^{SA}_f\\ G^{AS}_1 &= |\varepsilon| \quad G^{AS}_2 = |\varepsilon| - D^{AS}T \quad G^{SA} = |\varepsilon| - D^{SA}T\end{aligned}$$

$D^{f_1\to f_2} = \frac{C^{f_1\to f_2}}{Y}$, where $C^{f_1\to f_2}$ is the Clausius–Clapeyron constant for phase transformation from $\boldsymbol{f_1}$ to $\boldsymbol{f_2}$.

The conditional statements are

$$\mathcal{H}^{AM} = \begin{cases} 1, \text{if } \dot{T} < 0 \text{ and } T_f^{AM} \le T \le T_s^{AM} \\ 0, \text{otherwise} \end{cases}$$

$$\mathcal{H}_1^{AS} = \begin{cases} 1, \text{if } \begin{cases} \frac{D|\varepsilon|}{Dt} > 0 \text{ and } T \le T_S^{AM} \text{ and} \\ \frac{R_{s,1}^{AS}}{Y} + \varepsilon_L \xi_S \le |\varepsilon| \le \frac{R_{f,1}^{AS}}{Y} + \varepsilon_L \end{cases} \\ 0, \text{otherwise} \end{cases}$$

$$\mathcal{H}_2^{AS} = \begin{cases} 1, \text{if } \begin{cases} \frac{D(|\varepsilon| - D^{AS}T)}{Dt} > 0 \text{ and } T > T_S^{AM} \\ \frac{R_{s,2}^{AS}}{Y} + \varepsilon_L \xi_S \le |\varepsilon| - D^{AS}T \le \frac{R_{f,2}^{AS}}{Y} + \varepsilon_L \end{cases} \\ 0, \text{otherwise} \end{cases}$$

$$\mathcal{H}^{SA} = \begin{cases} 1, \text{if } \begin{cases} \frac{D(|\varepsilon| - D^{SA}T)}{Dt} < 0 \text{ and} \\ \frac{R_f^{SA}}{Y_A} \le |\varepsilon| - D^{SA}T \le \frac{R_s^{SA}}{Y} + \varepsilon_L \xi_S \end{cases} \\ 0, \text{otherwise} \end{cases}$$

Now, we aim to simplify and integrate these expressions so as to remove the time-dependence.

$$\dot{\xi}_S = \frac{(\xi_S - 1)\mathcal{H}_1^{AS}}{|\varepsilon| - S_{f,1}^{AS}} \frac{D|\varepsilon|}{Dt} + \left(\frac{(\xi_S - 1)\mathcal{H}_2^{AS}}{(|\varepsilon| - D^{AS}T) - S_{f,2}^{AS}} + \frac{\xi_S \mathcal{H}^{SA}}{(|\varepsilon| - D^{SA}T) - S_f^{SA}} \right) \frac{D(|\varepsilon| - D^{AS}T)}{Dt}$$

$$\dot{\xi}_M = \frac{(\xi_S + \xi_M - 1)\mathcal{H}^{AM}}{T - T_f^{AM}} \dot{T} + \frac{\xi_M \mathcal{H}_1^{AS}}{|\varepsilon| - S_{f,1}^{AS}} \frac{D|\varepsilon|}{Dt} + \left(\frac{\xi_M \mathcal{H}_2^{AS}}{(|\varepsilon| - D^{AS}T) - S_{f,2}^{AS}} + \frac{\xi_M \mathcal{H}^{SA}}{(|\varepsilon| - D^{SA}T) - S_f^{SA}} \right) \left(\frac{D(|\varepsilon| - D^{AS}T)}{Dt} \right)$$

Therefore,

$$d\xi_S = \frac{(\xi_S - 1)\mathcal{H}_1^{AS}}{|\varepsilon| - S_{f,1}^{AS}} d|\varepsilon| + \left(\frac{(\xi_S - 1)\mathcal{H}_2^{AS}}{(|\varepsilon| - D^{AS}T) - S_{f,2}^{AS}} + \frac{\xi_S \mathcal{H}^{SA}}{(|\varepsilon| - D^{SA}T) - S_f^{SA}} \right) (d|\varepsilon| - D^{AS}\, \mathrm{d}T)$$

$$d\xi_M = \frac{(\xi_S + \xi_M - 1)\mathcal{H}^{AM}}{T - T_f^{AM}} \mathrm{d}T + \frac{\xi_M \mathcal{H}_1^{AS}}{|\varepsilon| - S_{f,1}^{AS}} d|\varepsilon| + \left(\frac{\xi_M \mathcal{H}_2^{AS}}{(|\varepsilon| - D^{AS}T) - S_{f,2}^{AS}} + \frac{\xi_M \mathcal{H}^{SA}}{(|\varepsilon| - D^{SA}T) - S_f^{SA}} \right) (d|\varepsilon| - D^{AS}\, \mathrm{d}T)$$

By expanding the material derivative

$$\frac{D}{Dt} = \frac{\partial}{\partial t} + v \frac{\partial}{\partial s}$$

and considering steady state, we obtain

$$\mathcal{H}^{AM} = \begin{cases} 1, \text{if } \begin{cases} \frac{\partial T}{\partial s} < 0 \text{ and } T_f^{AM} \le T \le T_s^{AM} \end{cases} \\ 0, \text{otherwise} \end{cases}$$

$$\mathcal{H}_1^{AS} = \begin{cases} 1, \text{if } \begin{cases} \frac{\partial |\varepsilon|}{\partial s} > 0 \text{ and } T \le T_S^{AM} \text{ and} \\ \frac{R_{s,1}^{AS}}{Y} + \varepsilon_L \xi_S \le |\varepsilon| \le \frac{R_{f,1}^{AS}}{Y} + \varepsilon_L \end{cases} \\ 0, \text{otherwise} \end{cases}$$

$$\mathcal{H}_2^{AS} = \begin{cases} 1, \text{if } \begin{cases} \frac{\partial (|\varepsilon| - D^{AS}T)}{\partial s} > 0 \text{ and } T > T_S^{AM} \text{ and} \\ \frac{R_{s,2}^{AS}}{Y} + \varepsilon_L \xi_S \le |\varepsilon| - D^{AS}T \le \frac{R_{f,2}^{AS}}{Y} + \varepsilon_L \end{cases} \\ 0, \text{otherwise} \end{cases}$$

$$\mathcal{H}^{SA} = \begin{cases} 1, \text{if } \begin{cases} \frac{\partial (|\varepsilon| - D^{SA}T)}{\partial s} < 0 \text{ and} \\ \frac{R_f^{SA}}{Y_A} \le |\varepsilon| - D^{SA}T \le \frac{R_s^{SA}}{Y} + \varepsilon_L \xi_S \end{cases} \\ 0, \text{otherwise} \end{cases}$$

Bending

First, we consider when the wire is bent around the pulleys: $d|\varepsilon| > 0,\ \mathrm{d}T = 0, T \le T_S^{AM}$.

$$d\xi_S = \left(\frac{(\xi_S - 1)\mathcal{H}_1^{AS}}{|\varepsilon| - S_{f,1}^{AS}} + \frac{(\xi_S - 1)\mathcal{H}_2^{AS}}{(|\varepsilon| - D^{AS}T) - S_{f,2}^{AS}} + \frac{\xi_S \mathcal{H}^{SA}}{(|\varepsilon| - D^{SA}T) - S_f^{SA}} \right) d|\varepsilon|$$

$$d\xi_M = \left(\frac{\xi_M \mathcal{H}_1^{AS}}{|\varepsilon| - S_{f,1}^{AS}} + \frac{\xi_M \mathcal{H}_2^{AS}}{(|\varepsilon| - D^{AS}T) - S_{f,2}^{AS}} + \frac{\xi_M \mathcal{H}^{SA}}{(|\varepsilon| - D^{SA}T) - S_f^{SA}} \right) d|\varepsilon|$$

where the conditional statements simplify to

$$\mathcal{H}_1^{AS} = \begin{cases} 1, \text{if } \frac{R_{s,1}^{AS}}{Y} + \varepsilon_L \xi_S \le |\varepsilon| \le \frac{R_{f,1}^{AS}}{Y} + \varepsilon_L \\ 0, \text{otherwise} \end{cases}$$

$$\mathcal{H}_2^{AS} = 0$$

$$\mathcal{H}^{SA} = 0$$

If $\mathcal{H}_1^{AS} = 1$,

$$d\xi_S = \frac{(\xi_S - 1)}{|\varepsilon| - S_{f,1}^{AS}} d|\varepsilon| \ \ d\xi_M = \frac{\xi_M}{|\varepsilon| - S_{f,1}^{AS}} d|\varepsilon|$$

Hence,

$$\int_{\xi_{S,i}}^{\xi_S} \frac{d\xi_S}{(\xi_S - 1)} = \int_{\xi_{\epsilon,i}}^{\epsilon} \frac{d|\epsilon|}{\left(|\epsilon| - S_{f,1}^{AS}\right)}$$

$$\ln \frac{\xi_S - 1}{\xi_{S,i} - 1} = \ln \frac{|\varepsilon| - S_{f,1}^{AS}}{|\varepsilon_i| - S_{f,1}^{AS}}$$

$$\xi_S = \frac{|\varepsilon| - S_{f,1}^{AS}}{|\varepsilon_i| - S_{f,1}^{AS}}(\xi_{S,i} - 1) + 1$$

Similarly,

$$\xi_M = \frac{|\varepsilon| - S_{f,1}^{AS}}{|\varepsilon_i| - S_{f,1}^{AS}}\xi_{M,i}$$

Heating

Now, we consider the change due to heating: $\mathrm{d}T > 0,\ d|\varepsilon| = 0$

$$d\xi_S = -D^{AS}\left(\frac{(\xi_S - 1)\mathcal{H}_2^{AS}}{(|\varepsilon| - D^{AS}T) - S_{f,2}^{AS}} + \frac{\xi_S \mathcal{H}^{SA}}{(|\varepsilon| - D^{SA}T) - S_f^{SA}} \right)\mathrm{d}T$$

$$d\xi_M = \left[\frac{(\xi_S + \xi_M - 1)\mathcal{H}^{AM}}{T - T_f^{AM}} - D^{AS}\left(\frac{\xi_M \mathcal{H}_2^{AS}}{(|\varepsilon| - D^{AS}T) - S_{f,2}^{AS}} + \frac{\xi_M \mathcal{H}^{SA}}{(|\varepsilon| - D^{SA}T) - S_f^{SA}} \right)\right]\mathrm{d}T$$

where the conditional statements simplify to

$$\mathcal{H}^{AM} = 0$$

$$\mathcal{H}_2^{AS} = 0$$

$$\mathcal{H}^{SA} = \begin{cases} 1, \text{ if } \frac{R_f^{SA}}{Y_A} \le |\varepsilon| - D^{SA}T \le \frac{R_s^{SA}}{Y} + \varepsilon_L \xi_S \\ 0, \text{ otherwise} \end{cases}$$

If $\mathcal{H}^{SA} = 1$, then the above equations give

$$d\xi_S = -D^{AS}\frac{\xi_S}{(|\varepsilon| - D^{SA}T) - S_f^{SA}}\mathrm{d}T$$

$$d\xi_M = -D^{AS}\frac{\xi_M}{(|\varepsilon| - D^{SA}T) - S_f^{SA}}\mathrm{d}T$$

Therefore,

$$\xi_S = \frac{|\varepsilon| - D^{SA}T - S_f^{SA}}{|\varepsilon| - D^{SA}T_i - S_f^{SA}}\xi_{S,i}$$

$$\xi_M = \frac{|\varepsilon| - D^{SA}T - S_f^{SA}}{|\varepsilon| - D^{SA}T_i - S_f^{SA}}\xi_{M,i}$$

Hence, we reach the time-independent equations.

Characterisations

Convective coefficient

The value of convective coefficients is crucial in determining the temperature profile. In air, we heat the wire with an electrical current, and record the temperature drop via a thermal camera, and fit our experimental cooling data to the equation

$$T = T_o - (T_i - T_o)e^{-2\alpha}t \quad \alpha = \frac{h_a}{\rho\tau c}$$

as shown in Fig. 16, where T_o is the initial temperature of the wire and T_i the ambient temperature.

For the nitinol–water interface, we theoretically determine the convective coefficient by considering the cross section subjected to a constant temperature T_w at its surface $z = \tau$. Given the high thermal diffusivity $\alpha = k/(\rho c)$ and thin radius τ, we approximate temperature inside the cross section to be constant T_{mean}. From the heat equation, hence,

$$T_{\text{mean}} = \lim_{r_o \to 0} \frac{\int_{r_o}^{\tau} T[r,t](2\pi r)\, dr}{\pi\left(\tau^2 - r_o^2\right)}$$

Since

$$\dot{q} = \int \rho c \frac{dT_{\text{mean}}}{\mathrm{d}t}\, dA = h_w A(T_w - T_{\text{mean}})$$

, the gradient of heat gain $\dot{q}$ against $T_w - T_{\text{mean}}$ graph equals $h_w \cdot A$, where h_w is the convective coefficient of nitinol in water, and the surface area $A = 2\pi\tau$.

Moment of inertia

We construct a pendulum by attaching a bob of known mass and radius to the pulleys, which are given a small displacement (Fig. 17).

The period of a pendulum is defined as

$$T = 2\pi\sqrt{\frac{I_{\text{total}}}{m_{\text{total}} g r_{\text{cm}}}}$$

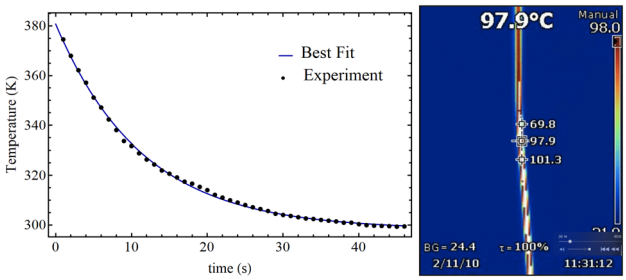

Fig. 16 Cooling curve of nitinol wire in air (points) with best-fit line, [right] thermal camera footage

Fig. 17 Image of setup used to characterise moment of inertia of pulleys, by attaching a weight of known mass

where r_{cm} is the distance from the centre of mass to rotational axis. Here, $m_{\text{total}} = m_b + m_p$, $r_{\text{cm}} = \dfrac{m_b}{m_{\text{total}}} d$,

where m_b, m_p are the mass of the bob and pulley, and d is the distance from CM of bob to centre of pulley (rotational axis). Hence, by parallel axis theorem,

$$\omega = \sqrt{\frac{mgd}{I_o + I_{\text{ball}} + md^2}}$$

We perform a fast fourier transform on the Tracker-obtained data, to obtain the experimental ω, which we use to characterise the moment of inertia I_o.

Frictional coefficient

From the equation

$$I\ddot{\theta} = -k_f - k_s\dot{\theta}$$

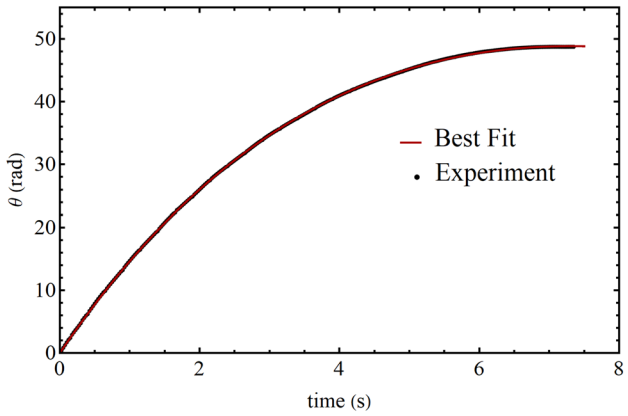

Fig. 18 Experimental plot of angle θ against time (red), with theoretical fit (blue)

where k_f and k_s are the coefficients of torque for (constant) friction and (linear) shear drag, we arrive at the equation.

$$\theta[t] = -\frac{k\left(1 - e^{-k_f t}\right) - k_s t}{k_f}$$

where k is a constant of integration. To characterise the unknown coefficients, we use Tracker to follow the motion of a point on the pulley for an unpowered spin down, obtaining a graph of angle rotated against time. Fitting the theoretical equation to the experimental data will return three unknowns, k, k_s, k_f (Fig. 18).

Temperature for phase transformation

The differential scanning calorimeter returns the curve of heat flux against temperature during heating (blue) and cooling (yellow) for a heating-cooling cycle. Using the tangent line method, we determine the temperature for phase transformation (Fig. 19).

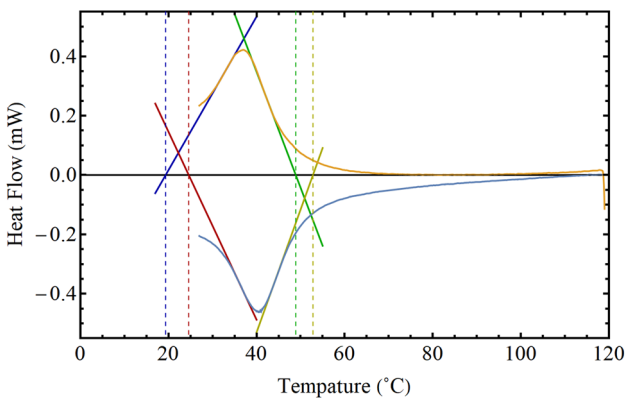

Fig. 19 Tangent lines and points of intersection with x-axis

Knowing the start and final temperatures for phase transformations between martensite and austenite, we achieve a phase plot of stress against temperature (Fig. 10 of paper). Phase transformations occur within the shaded regions, and the three phases coexist within the unlabelled region, while only the specific phase is present in the labelled regions.

Acknowledgements The authors would like to thank Mr. Joel Tan Shi Quan from Yong Loo Lin School of Medicine, and NUS High School of Mathematics and Science for their invaluable guidance and support, as well as Dr. Yoanna A. Kurnianingsih for comments on the manuscript.

Declarations

Conflict of interest The authors declare that they have no conflict of interest.

References

1. K. Otuka, X. Ren, Physical metallurgy of Ti-Ni-based shape memory alloys. Prog. Mater. Sci. **50**(5), 511–678 (2005)
2. P.G. McCormick, Shape memory effect heat engine performance. Appl. Energy **24**(3), 221–243 (1986)
3. T. Uehara, Molecular dynamics simulation of shape-memory behavior. Shape Mem. Alloy. 10–17 (2010)
4. T. Sato, Molecular dynamics study on nano structure and shape-memory property of Ni-Ti alloy. Trans. Mat. Res. Soc. Japan **29**, 3615–3618 (2004)
5. G.J. Ackland, A.P. Jones, R. Noble-Eddy, Molecular dynamics simulations of the martensitic phase transition process. Mater. Sci. Eng. A **481**, 11–17 (2008)
6. J. Zurbitu, S. Kustov, A. Zabaleta, E. Cesari, J. Aurrekoetxea, *Thermo-Mechanical Behaviour of NiTi at Impact (In Shape Memory Alloys*), (IntechOpen, 2010)
7. D. Stoeckel, Nitinol medical devices and implants. Minim. Invas. Therapy Allied Technol. **9**(2), 81–88 (2000)
8. H. Luo, E. Abel, X. Liu, Y. Liao, Z. Wang, *Hysteresis Behaviour and Modeling of SMA Actuators*. (In Shape Memory Alloys, IntechOpen, 2010)
9. R. Banks, The banks engine. Naturwissenschaften **62**(7), 305–308 (1975)
10. J.J. Zhu, N.G. Liang, K.M. Liew, W.M. Huang, Energy conversion in shape memory alloy heat engine part i: Theory. J. intell. Mater. Syst. Struct. **12**(2), 127–132 (2001)
11. R. Salzbrenner, Shape memory heat engines. J. Mater. Sci. **19**(6), 1827–1835 (1984)
12. Y. Chemisky, A. Duval, E. Patoor, T.B. Zineb, Constitutive model for shape memory alloys including phase transformation, martensitic reorientation and twins accommodation. Mech. Mater. **43**(7), 361–376 (2011)
13. R. Rizzoni, S. Marfia, A thermodynamical formulation for the constitutive modeling of a shape memory alloy with two martensite phases. Meccanica **50**(4), 1121–1145 (2015)
14. C. Yang, S. Abanteriba, A. Becker, A review of shape memory alloy based filtration devices. AIP Adv. **10**(6), 060701 (2020)
15. M. Batista, Elastic belt extended by two equal rigid pulleys. Acta Mech. **230**(11), 3825–3838 (2019)
16. B.T. Berg, Bending of superelastic wires, Part I: experimental aspects. J. Appl. Mech. **62**, 459–465 (1995)
17. F. Auricchio, E. Sacco, A temperature-dependent beam for shape-memory alloys: constitutive modelling, finite-element implementation and numerical simulations. Comput. Methods Appl. Mech. Eng. **174**(1–2), 171–190 (1999)
18. A. Ben-Israel, A Newton-Raphson method for the solution of systems of equations. J. Math. Anal. Appl. **15**(2), 243–252 (1966)
19. G.J. Suppes, T.S. Storvick, Sustainable Power Technologies and Infrastructure: The New Electric Vehicle Society, (Academic Press, 2016), pp. 161–190